Laser & Photonics Reviews

LASER & PHOTONICS REVIEWS

www.lpr-journal.org

RESEARCH ARTICLE

Observation of Klein Tunneling in Antichiral Gyromagnetic Photonic Crystals

Qiutong Zhen[1] | Chunquan Peng[1] | Yujie Tang[1] | Yutian Ao[2] | Qindong Xie[1] | Xiaowei Wang[1] | Yuan Chen[1] | Gui-Geng Liu[3] | Peiheng Zhou[1]

[1]National Engineering Research Center of Electromagnetic Radiation Control Materials, Key Laboratory of Multi-spectral Absorbing Materials and Structures of Ministry of Education, University of Electronic Science and Technology of China, Chengdu, China | [2]Division of Physics and Applied Physics, School of Physical and Mathematical Sciences, Nanyang Technological University, Singapore | [3]Department of Electronic and Information Engineering, School of Engineering, Westlake University, Hangzhou, China

Correspondence: Gui-Geng Liu (liuguigeng@westlake.edu.cn) | Peiheng Zhou (phzhou@uestc.edu.cn)

Received: 13 May 2026 | **Revised:** 5 July 2026 | **Accepted:** 10 July 2026

Keywords: antichiral gyromagnetic photonic crystals | defect-tolerant transport | Klein Tunneling | magnetic-bias-induced potential barriers

ABSTRACT

As a non-classical transport behavior within relativistic quantum mechanics, the Klein tunneling effect is fundamentally characterized by the perfect transmission of particles traversing a classical potential barrier under normal incidence. Although this effect has been demonstrated in electronic, phononic, and photonic platforms, its experimental realization in gyromagnetic photonic crystals remains largely unexplored. Such systems offer a distinct route to constructing effective potential barriers through magnetic-bias tuning. In this work, we experimentally demonstrate Klein tunneling in an antichiral gyromagnetic photonic crystal. Utilizing Dirac cones with an intrinsic frequency offset between the *K* and *K'* valleys, we construct a *K*-valley heterojunction by reversing the local magnetic fields. Microwave near-field measurements reveal high transmission through the heterojunction, accompanied by planar phase fronts and momentum-space signatures consistent with *K*-valley transport. Both simulations and experiments verify the insensitivity of this phenomenon to variations in the height and width of the potential barrier. Furthermore, Klein tunneling within this architecture exhibits robustness against both bulk and edge defects. This work thus provides new design paradigms for novel topologically protected transport devices.

1 | Introduction

When massless relativistic particles traverse a classical potential barrier, they can achieve perfect transmission under normal incidence, irrespective of the barrier's height and width. This counterintuitive transport behavior was theoretically demonstrated by Oskar Klein in 1929 and is widely recognized as Klein tunneling [1]. Although the direct observation of this phenomenon in elementary particle systems is extremely challenging [2], the emergence of artificial macroscopic materials exhibiting Dirac-like dispersions has provided highly controllable platforms for its physical realization [3]. To date, Klein tunneling has been indirectly verified in condensed matter electronic systems [4, 5], specifically via massless Dirac fermions in graphene [6]. The experimental verification of this intriguing phenomenon has been extended to classical-wave systems, including phononic crystals [7–12] and valley photonic crystals [13, 14]. Furthermore, phenomena such as super-Klein tunneling of spin-1 particles [15, 16], anti-Klein tunneling of chiral particles [17, 18], and the Klein tunneling of massive particles [19] have also been observed in artificial materials, thereby expanding the family of Klein transport phenomena. However, the experimental observation of this perfect transmission within gyromagnetic photonic crystals (GPCs) has not been realized.

GPCs, which break time-reversal symmetry, have emerged as a crucial physical platform for realizing classical-wave topological phenomena [20]. Research on topological GPCs has primarily focused on topologically protected boundary effects, such as unidirectional chiral edge states [21–23], surface states [24, 25], and hinge states [26, 27]. In contrast, the exploration of unconventional bulk transport in gyromagnetic systems remains considerably limited, especially when robust transmission, broad bandwidth, and large effective area are required simultaneously [28–30]. The experimental realization of antichiral gyromagnetic photonic crystals (AGPCs)—derived from the modified Haldane model—provides a promising route to address this challenge [31, 32]. Here, "antichiral" refers to the modified-Haldane-type valley-dependent band structure and its associated edge-transport characteristics, rather than to geometrical chirality. Characterized by Dirac cones with an intrinsic energy offset [33], the unique band structure of AGPCs offers a platform for investigating unconventional bulk transport. For example, researchers have further realized unidirectional bulk states [34], topological antennas [35], and hybrid edge states [36–38]. Crucially, such intrinsic energy offset provides direct inspiration for constructing macroscopic potential barriers: simply reversing the magnetic field applied to each sublattice in an AGPC establishes an equivalent energy barrier on a single Dirac cone, without necessitating any modifications to the structural dimensions of the lattice. Consequently, this framework serves as a natural and highly tunable platform for the experimental exploration of Klein tunneling and unconventional bulk transport in GPCs.

In this work, we report the first experimental observation of Klein tunneling in an AGPC system. By precisely modulating the magnetic fields applied to the two sublattices within a hexagonal lattice, we have realized a modified Haldane model in a photonic architecture as reported previously [31]. Here, by locally reversing the magnetic field across a designated section of the array, we constructed a macroscopic K-point heterojunction with a designated potential barrier. Utilizing a plane-wave feed for microwave near-field measurements, we observed high transmittance across the heterojunction. The occurrence of Klein tunneling was confirmed through the analysis of the transmission spectra, the electric field phase distributions, and the spatial Fourier transforms. Both numerical simulations and experimental results collectively verify that, under normal incidence, the near-perfect transmission is insensitive to variations in both the height and width of the constructed potential barrier. Furthermore, we investigated the unique properties of AGPCs associated with Klein tunneling: by deliberately introducing bulk defects within the barrier or edge defects along the architecture boundaries, we demonstrated the robust defect immunity of the bulk transport. Ultimately, these findings translate the fundamental physics of Klein tunneling into a practical macroscopic platform, establishing a blueprint for topological transport devices featuring large-area, broadband, and defect-immune capabilities.

2 | Results and Discussion

The photonic Klein-tunneling system based on the AGPC heterojunction and the corresponding wave-transport process are illustrated in Figure 1a. A potential barrier with a frequency difference of V and a length of L is located at the center of the array. Normally incident massless Dirac particles encountering this barrier will undergo perfect transmission theoretically (The theoretical derivation demonstrating the perfect transmission of massless Dirac particles through the heterojunction under normal incidence is provided in Section S1). To elucidate the design scheme of such a system, we illustrate the arrangement of the 2D photonic honeycomb lattices in Figure 1b. The heterojunction primarily consists of two types of AGPC lattices, designated as Type-A and Type-B. The magnetic fields applied to each gyromagnetic cylinder in sublattices A and B are oppositely configured to exhibit an in-plane antiferromagnetic distribution (Detailed electromagnetic parameters of the utilized gyromagnetic YIG rods are provided in Section S3). The experimental implementation of the AGPC lattice is depicted in Figure 1c,d, where the gyromagnetic cylinders are sandwiched between two parallel metal plates to support an in-plane TM mode. Subsequently, NdFeB permanent magnets are positioned within a custom-designed PVC template to magnetize the YIG rods with a magnetic field $B = 0.09$ T.

Under the influence of the staggered magnetic bias, each honeycomb lattice exhibits properties predicted by the modified Haldane model: The Dirac cones at the K and K' valleys exhibit a distinct intrinsic frequency offset. Numerically, the Type-A lattice exhibits a Dirac frequency of 6.98 GHz at the K valley and 7.72 GHz at the K' valley, as shown in Figure 1e. Such a frequency offset plays the role of an effective potential barrier. By reversing the local magnetic-bias direction of the sublattices, the numerically simulated dispersion in Figure 1f reveals an exactly reversed frequency offset between the K and K' valleys for the Type-B lattice. Consequently, an effective scalar potential barrier with $V = 0.74$ GHz is constructed for the K valley in the A-B-A heterojunction. A convenient physical platform is thus built to investigate the transport behavior of massless Dirac particles. The theoretical derivation of the effective Dirac description of the AGPC and the resulting magnetic-bias-induced potential barrier is provided in Section S2.

First, we set the length of the potential barrier to $L = 5a_x$, and configure the Klein tunneling strip sample with a length of $12a_x$ (Type-A) $+5a_x$ (Type-B) $+12a_x$ (Type-A), a width of $18a_y$ (see Figure 2a). To support bulk state transmission, a plane-wave source composed of 32 point sources is positioned within the lattice. Then, microwave near-field scanning is conducted through the whole sample. During measurements, the sample edges are covered with microwave absorbers to eliminate the impact of interfacial reflections and leaky waves. Detailed information regarding the scanning environment and the calibration results for the plane wave generated by the point-source array is provided in Sections S7 and S8, respectively. The simulated angular dependence of the field-transmission metric, further validating the effective plane-wave excitation used in the experiment, is provided in Section S9. Along the length, we define three equal-sized regions—labeled I, II, and III (each with a length of $5a_x$ and width of $12a_y$)—located within the Type-A, Type-B, and Type-A regions of the heterojunction, respectively. Thereafter, the transmission coefficient is obtained as [7]:

$$T = \frac{\iint_{III} |E_z|\, ds}{\iint_{I} |E_z|\, ds} \tag{1}$$

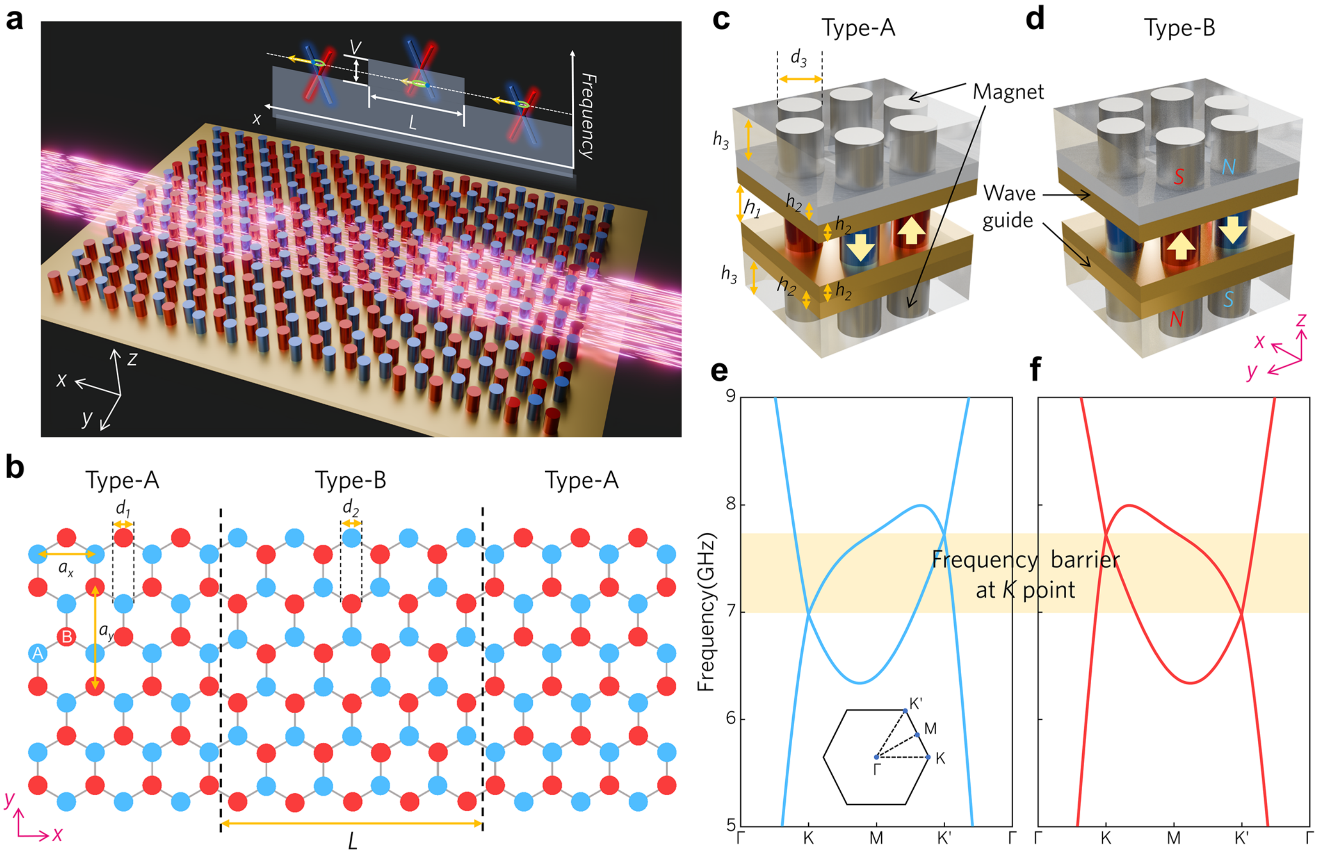

FIGURE 1 | Architecture and operating principle of the AGPC heterojunction for Klein tunneling. (a) Schematic of the Klein tunneling system and the wave-transport process. The yellow arrows denote the direction of particle motion. The cover plate of perfect electric conductor (PEC) is removed for visualization of the structure, while the PEC bottom plate is retained. The red and blue cylinders are gyromagnetic materials oppositely biased by magnetic fields. (b) Configuration of the 2D AGPC heterojunction array in (a), where L denotes the length of the barrier region. The honeycomb lattice is composed of gyromagnetic cylinders with diameters $d_1 = d_2 = 4.4$ mm. The lattice constants are $a_x = 12$ mm, $a_y = \sqrt{3}a_x$. Sublattices A and B correspond to the blue and red dots respectively. (c) Physical realization and (e) corresponding numerical band structure of the Type-A AGPC lattice. (d) Physical realization and (f) corresponding numerical band structure of the Type-B AGPC photonic lattice. The AGPC lattices are embedded in a parallel-plate copper waveguide with a thickness of $h_2 = 2$ mm. The yttrium iron garnet (YIG) rods with a height of $h_1 = 6$ mm are magnetized by permanent magnets with a diameter of $d_3 = 5$ mm. Two PVC templates with a thickness of $h_3 = 5$ mm are introduced to fix magnets. The yellow arrows indicate the directions of the applied magnetic fields.

where $|E_z|$ is the amplitude of the electric field and the integrals are applied over the predefined regions. A comparison of the field and power transmission coefficient, showing consistent spectral behavior, is provided in Section S4.

Note that the large sample width is designed to ensure: 1) momentum conservation along the width direction under normal incidence, and 2) consistency of the transmission spectra when comparing periodic boundary conditions with open boundary conditions terminated by perfectly matched layers (PML) along the width direction. (Detailed simulations of the transmission spectra for both the sample with finite width and the ideal model with infinite width are provided in Section S5). However, such a configuration inevitably amplifies the influence of the inherent electromagnetic losses associated with the gyromagnetic YIG material. To address this, we evaluate the impact of material's dielectric and magnetic losses on the transmission spectra for both the sample and the ideal infinitely wide model in Section S6. The numerical results demonstrate that these intrinsic material losses do not alter the overall trend of the transmission spectra, in other words, the overall physics.

Indeed, the measured transmission spectra, depicted in Figure 2b, reveal high transmittance across both the pre-offset (below 6.98 GHz) and offset (6.98–7.72 GHz) regimes in frequency domain. However, the transmission coefficient drops precipitously once the frequency exceeds the high-frequency Dirac point and enters the nonlinear dispersion region. Furthermore, the numerically simulated transmission spectra exhibit a highly consistent trend with the experimental data.

To further elucidate the bulk transport, we present the near-field scanning results of the electric field amplitude $|E_z|$ in the pre-offset (6.62 GHz), offset (7.42 GHz), and nonlinear dispersion region (7.84 GHz) in Figure 2c-e. At 6.62 GHz, the electric field is uniformly distributed across regions I, II, and III. In contrast, the electric field remains uniform in regions I and III, but exhibits a distinct oscillatory pattern in region II—a hallmark field distribution of Klein tunneling at 7.42 GHz.

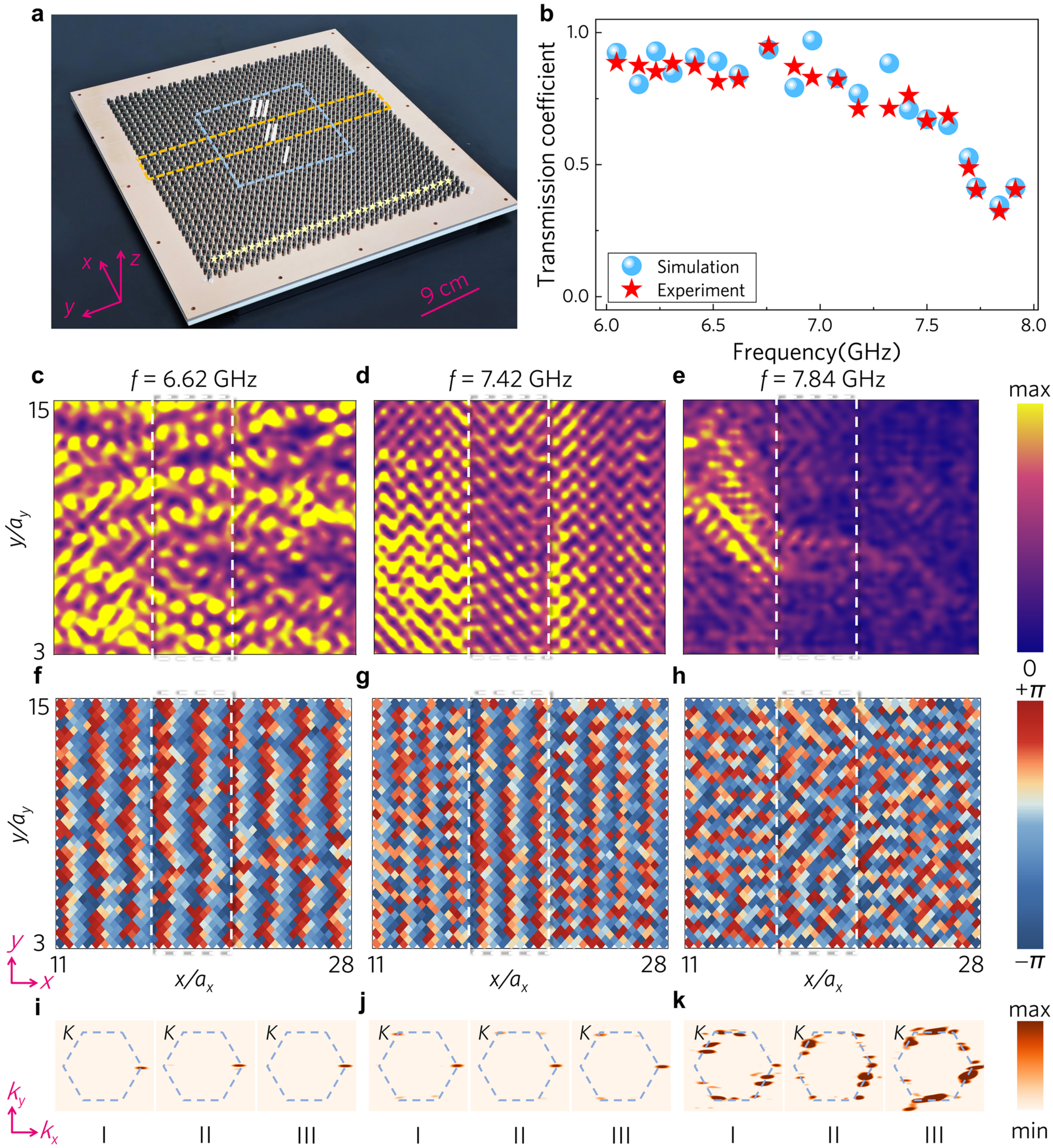

FIGURE 2 | Experimental observation of Klein tunneling in the AGPC heterojunction. (a) Photograph of the fabricated AGPC heterojunction sample. The sample spans $18a_y$ in the y-direction, while its x-direction length is divided into three segments of $14a_x$, $5a_x$, and $12a_x$. Yellow asterisks denote the discrete point sources, positioned along a line parallel to y-axis at $x = 2a_x$. Labels I, II, and III designate the spatial regions before, within, and after the potential barrier, respectively. (b) Simulated and experimentally measured frequency-domain transmission spectra across the barrier. (c–k) Measured spatial distributions of the electric field amplitude $|E_z|$ (c–e), corresponding phase profiles (f–h), and spatial Fourier transformed spectra (i–k). These panels systematically map the field evolutions at frequencies below the barrier (6.62 GHz, c,f,i), within the barrier (7.42 GHz, d,g,j), and above the barrier (7.84 GHz, e,h,k). The white dashed box delineates the potential barrier region, and the blue dashed hexagons indicate the first Brillouin zones.

Figure 2f-h displays the corresponding phase profiles of E_z for these three cases. The phase profiles for the pre-offset and offset cases clearly confirm that the electromagnetic waves maintain a planar wavefront along the length direction, thereby conserving their transverse momentum along the width direction (parallel to the interface). In the nonlinear region, the phase-matching condition between the incident wave and the Bloch modes supported by the AGPC heterojunction is no longer satisfied, resulting in a severely distorted phase distribution and preventing the wave from crossing the potential barrier [39]. Finally, we analyze the electromagnetic wave transport in k-space. The spatial Fourier transformed spectra of the measured E_z fields,

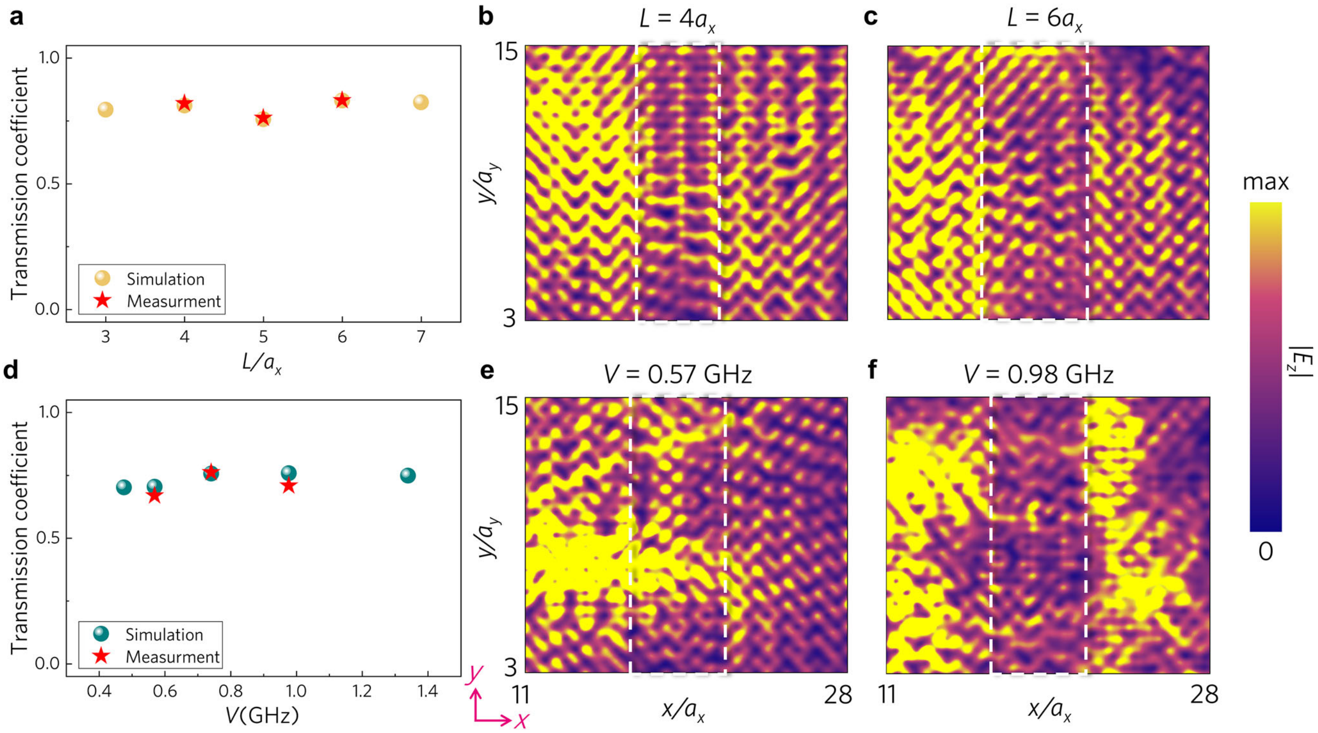

FIGURE 3 | Insensitivity of Klein transport in the AGPC heterojunction to the width and height of the potential barrier. (a,d) Simulated and experimental transmission spectra of the AGPC heterojunction as a function of (a) barrier width and (d) barrier height. (b,c) Measured near-field electric field amplitude ($|E_z|$) distributions for barrier widths of $L = 4a_x$ and $L = 6a_x$, respectively. (e,f) Corresponding measured $|E_z|$ distributions for barrier potentials of $V = 0.57$ GHz and $V = 0.98$ GHz, respectively. Here, L is fixed at $5a_x$. The white dashed boxes delineate the barrier regions. All simulations and measurements were performed at an operating frequency of $f = 7.4$ GHz.

shown in Figure 2i–k, reveal that the plane waves are excited exclusively along the Γ–K direction within the first Brillouin zone of the AGPC heterojunction (1D k_x Fourier spectra are provided in Section S10). This observation further confirms the validity of our K-point barrier construction methodology. Based on all the aforementioned measurement data, we confirm the experimental observation of Klein tunneling within the AGPC heterojunction system.

Klein tunneling features not only the high transmission through a potential barrier but also the invariance of this property relative to the barrier's width and height. Here, we verify such invariance in our AGPC heterojunction system. To vary the barrier width, adjustments are implemented directly by modulating the width of Region II. At 7.4 GHz, Figure 3a illustrates the relationship between the transmission coefficient and the barrier width L, where the numerical simulations and experimental data exhibit agreement, thereby confirming the barrier width-independent nature of Klein tunneling in AGPC heterojunctions. Figure 3b,c present the near-field scanning results of $|E_z|$ for $L = 4a_x$ and $6a_x$, respectively. It is evident that the incident plane waves traverse the barrier without mode conversion, maintaining consistency with the mode profile shown in Figure 2d.

Next, we vary the barrier height by modifying the diameter of the YIG rods in Region II. Detailed simulations of barrier-height tuning through the YIG rod diameter, including the resulting K-valley Dirac frequency and interface-normal Dirac velocity, are provided in Section S11. Figure 3d displays the transmission spectra as a function of the barrier height V, showing high consistency between simulations and experiments, which further validates the height-insensitivity of Klein tunneling in this system. Figure 3e,f depict the $|E_z|$ field maps for $V = 0.57$ GHz ($d_2 = 4.8$ mm) and 0.98 GHz ($d_2 = 4$ mm), respectively. As the barrier height increases, the mismatch between the mode profile in Region II and those in Regions I and III becomes more pronounced. Notably, as the displayed field modes are all measured at 7.4 GHz, a frequency approaching the nonlinear dispersion region, a slight reduction in the transmission coefficient is therefore introduced.

A key advantage of topological phases is their robustness against structural defects. To distinguish our system from heterojunctions constructed via conventional massless Dirac points, we deliberately introduced various types of defects into the AGPC heterojunction to investigate the robustness of our Klein tunneling transport. First, by applying twisted boundary conditions [40], we evaluate the topological properties of the AGPC heterojunction (detailed results are provided in Section S12), confirming that the topological characteristics inherited from graphene [33] are rigorously preserved. Subsequently, we introduce a bulk defect within Region II by removing an entire honeycomb lattice unit cell, as depicted in Figure 4a. Despite this substantial structural perturbation, the near-field scanning results of $|E_z|$ in Figure 4c remain the hallmark mode distribution of Klein tunneling, accompanied by a highly localized resonant mode within the air cavity.

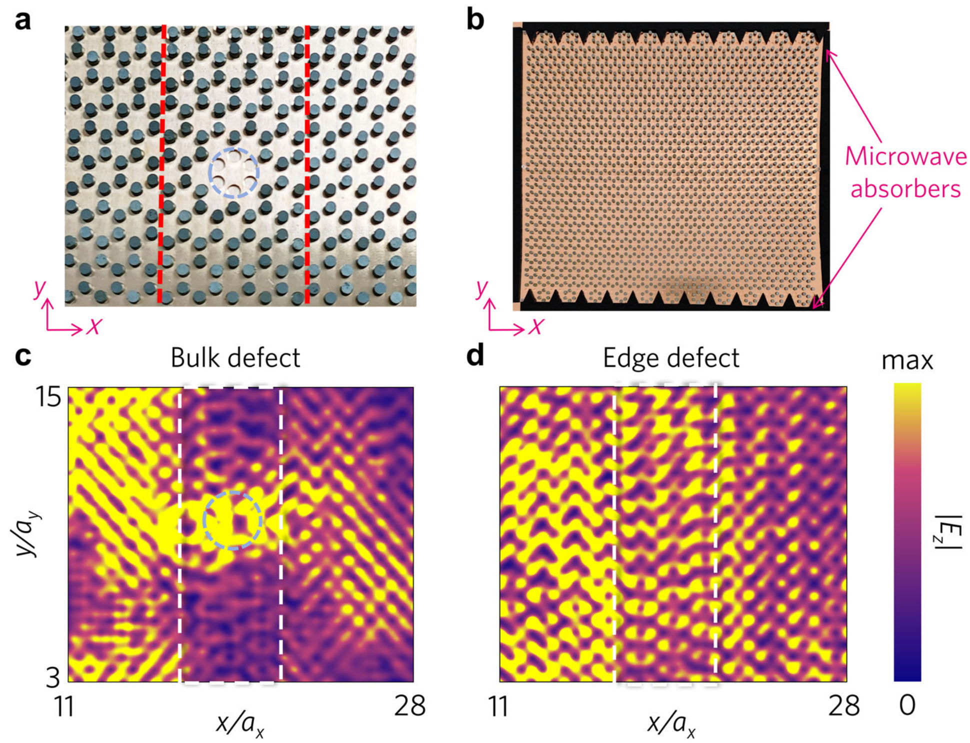

FIGURE 4 | Defect immunity of Klein tunneling in the AGPC heterojunction. (a,b) Photographs of the fabricated AGPC heterojunctions featuring (a) a deliberately introduced bulk defect and (b) edge defect. (c,d) Corresponding measured near-field electric field amplitude ($|E_z|$) distributions for the bulk (c) and edge (d) defect configurations. The blue dashed lines outline the introduced bulk defect, while the red dashed lines and white dashed boxes delineate the boundaries and Region II, respectively. All measurements were conducted at an operating frequency of $f = 7.4$ GHz.

Furthermore, we experimentally observed the antichiral edge state signatures typical of the modified Haldane model within the proposed heterojunction (detailed experimental results are presented in Section S13). This observation prompted an intriguing physical question: would disrupting the physical boundaries of the heterojunction compromise its bulk transmission capabilities? To address this, we introduced a novel type of imperfection—termed an "edge defect"—by periodically removing selected unit-cells along the heterojunction boundaries and filling the resulting voids with microwave absorbers, as illustrated in Figure 4b. The corresponding $|E_z|$ near-field map in Figure 4d indicates that a high-transmission bulk response remains observable under the tested boundary perturbations. These measurements establish the experimentally tested defect response of Klein-tunneling transport in the AGPC heterojunction.

3 | Conclusions

In conclusion, we have reported the first experimental observation of Klein tunneling within an AGPC system. Exploiting the frequency offset of Dirac cones inherent to the modified Haldane model, we successfully constructed a macroscopic K-point heterojunction within an AGPC simply by locally reversing the applied magnetic field. Microwave near-field measurements of the proposed heterojunction—transmission spectra, electric field amplitude and phase distributions, as well as spatial Fourier analysis—confirmed the high transmittance of normally incident electromagnetic waves across the potential barrier. Furthermore, by demonstrating the insensitivity of this transport mechanism to variations in both the height and width of the barrier, we systematically verified the core physical hallmarks of Klein tunneling. Crucially, the system exhibited robustness: the bulk state transmission was remarkably preserved even under structural perturbations, including artificially introduced bulk defects within the barrier region and edge defects.

Compared with representative classical-wave Klein-tunneling platforms, which predominantly employ geometrically induced barriers, the present work combines a time-reversal-symmetry-broken platform, geometry-preserving magnetic-bias-induced barrier construction, and experimentally tested defect response (detailed comparison is presented in Section S14). Analogous Klein tunneling may also be explored in time-reversal-invariant bianisotropic photonic insulators [39] and photonic semimetals [41]. This work not only deepens the fundamental understanding of unconventional bulk state propagation mechanisms in time-reversal-symmetry-broken media but also broadens the experimental paradigms for simulating relativistic quantum phenomena in classical wave systems. Moreover, it provides novel strategies for the design of topological nonreciprocal devices [39], advanced signal modulation platforms [42], and robust broadband high-throughput components in 2D and 3D platforms [13, 28–30, 43].

Acknowledgements

P.Z. acknowledges funding from National Natural Science Foundation of China Grant Nos. 52425205 and 52021001. G.-G.L. acknowledges funding from Research Center for Industries of the Future (RCIF) at Westlake

University Grant Number 210000006022312 and Westlake Education Foundation Grant Number 103110736022301.

Conflicts of Interest

The authors declare no conflicts of interest.

Data Availability Statement

The data that support the findings of this study are available from the corresponding author upon reasonable request.

References

1. O. Klein, "Die Reflexion von Elektronen an einem Potentialsprung nach der Relativistischen Dynamik von Dirac," *Zeitschrift für Physik* 53, no. 3 (1929): 157–165, https://doi.org/10.1007/BF01339716.

2. A. Calogeracos and N. Dombey, "History and Physics of the Klein Paradox," *Contemporary Physics* 40, no. 5 (1999): 313–321, https://doi.org/10.1080/001075199181387.

3. C. T. Chan, Z. H. Hang, and X. Huang, "Dirac Dispersion in Two-Dimensional Photonic Crystals," *Advances in OptoElectronics* 1 (2012): 313984.

4. P. E. Allain and J.-N. Fuchs, "Klein Tunneling in Graphene: Optics With Massless Electrons," *The European Physical Journal B* 83, no. 3 (2011): 301–317, https://doi.org/10.1140/epjb/e2011-20351-3.

5. M. I. Katsnelson, K. S. Novoselov, and A. K. Geim, "Chiral Tunnelling and the Klein Paradox in Graphene," *Nature Physics* 2, no. 9 (2006): 620–625, https://doi.org/10.1038/nphys384.

6. C. Gutiérrez, L. Brown, C. Kim, J. Park, and A. Pasupathy, "Klein Tunnelling and Electron Trapping in Nanometre-Scale Graphene Quantum Dots," *Nature Physics* 12, no. 11 (2016): 1069–1075.

7. X. Jiang, C. Shi, Z. Li, et al., "Direct Observation of Klein Tunneling in Phononic Crystals," *Science* 370, no. 6523 (2020): 1447–1450, https://doi.org/10.1126/science.abe2011.

8. N. Gao, J. Wang, and W. Chen, "Klein Tunneling for Lamb Waves in Elastic Phononic Crystal Plates," *Applied Physics Letters* 121, no. 10 (2022): 102201, https://doi.org/10.1063/5.0105897.

9. K. Chen, X. Dong, P. Gao, et al., "Multifunctional Applications of Topological Valley-Locked Elastic Waves," *International Journal of Mechanical Sciences* 259 (2023): 108589, https://doi.org/10.1016/j.ijmecsci.2023.108589.

10. D. Lee, Y. Jiang, X. Zhang, et al., "Klein Tunneling of Gigahertz Elastic Waves in Nanoelectromechanical Metamaterials," *Device* 2, no. 10 (2024): 100474.

11. G. Yu, J. Xie, S. Gao, et al., "Reconfigurable Directional Selective Tunneling of p-type Phonons in Polarized Elastic Wave Systems," *Materials & Design* 245 (2024): 113262, https://doi.org/10.1016/j.matdes.2024.113262.

12. Y. Yao, Y. Ma, F. Hong, et al., "On Klein Tunneling of Low-Frequency Elastic Waves in Hexagonal Topological Plates," *Applied Mathematics and Mechanics* 45, no. 7 (2024): 1139–1154, https://doi.org/10.1007/s10483-024-3163-9.

13. M. Gupta, A. Kumar, P. Pitchappa, et al., "150 Gbps THz Chipscale Topological Photonic Diplexer," *Advanced Materials* 36, no. 19 (2024): 2309497, https://doi.org/10.1002/adma.202309497.

14. W. Li, Q. Chen, Y. Sun, et al., "Topologically Enabled On-Chip THz Taper-Free Waveguides," *Advanced Optical Materials* 11, no. 21 (2023): 2300764, https://doi.org/10.1002/adom.202300764.

15. Y. Zhu, A. Merkel, L. Cao, et al., "Experimental Observation of Super-Klein Tunneling in Phononic Crystals," *Applied Physics Letters* 122, no. 21 (2023): 211701, https://doi.org/10.1063/5.0151336.

16. H. Wu, H. He, Z. Dong, et al., "Super Klein Tunneling in Phononic Lieb Lattices," *Physical Review Applied* 21, no. 3 (2024): 034026, https://doi.org/10.1103/PhysRevApplied.21.034026.

17. M. M. Elahi, H. Vakili, Y. Zeng, C. R. Dean, and A. W. Ghosh, "Direct Evidence of Klein and Anti-Klein Tunneling of Graphitic Electrons in a Corbino Geometry," *Physical Review Letters* 132, no. 14 (2024): 146302, https://doi.org/10.1103/PhysRevLett.132.146302.

18. H. Li, Y. Liu, Q. Ding, et al., "Observation of Anti-Klein Tunneling of Chiral Phonons," *Science Bulletin* 70, no. 15 (2025): 2407–2410, https://doi.org/10.1016/j.scib.2025.05.024.

19. L. Yu, H. Xue, R. Guo, et al., "Dirac Mass Induced by Optical Gain and Loss," *Nature* 632, no. 8023 (2024): 63–68, https://doi.org/10.1038/s41586-024-07664-x.

20. L. Lu, J. D. Joannopoulos, and M. Soljačić, "Topological Photonics," *Nature Photonics* 8, no. 11 (2014): 821–829, https://doi.org/10.1038/nphoton.2014.248.

21. Z. Wang, Y. Chong, J. D. Joannopoulos, and M. Soljacic, "Observation of Unidirectional Backscattering-Immune Topological Electromagnetic States," *Nature* 461, no. 7265 (2009): 772–775, https://doi.org/10.1038/nature08293.

22. S. A. Skirlo, L. Lu, and M. Soljačić, "Multimode One-Way Waveguides of Large Chern Numbers," *Physical Review Letters* 113, no. 11 (2014): 113904, https://doi.org/10.1103/PhysRevLett.113.113904.

23. Y. Jing, Y. Yang, W. Long, et al., "Experimental Realization of Highly Efficient Beam Combination and Steering via Topological Multimode," *Laser & Photonics Reviews* 19, no. 11 (2025): 2401157, https://doi.org/10.1002/lpor.202401157.

24. G.-G. Liu, Z. Gao, Q. Wang, et al., "Topological Chern Vectors in Three-Dimensional Photonic Crystals," *Nature* 609, no. 7929 (2022): 925–930, https://doi.org/10.1038/s41586-022-05077-2.

25. X. Xi, B. Yan, L. Yang, et al., "Topological Antichiral Surface States in a Magnetic Weyl Photonic Crystal," *Nature Communications* 14, no. 1 (2023): 1991, https://doi.org/10.1038/s41467-023-37710-7.

26. G.-G. Liu, S. Mandal, X. Xi, et al., "Photonic Axion Insulator," *Science* 387, no. 6730 (2025): 162–166, https://doi.org/10.1126/science.adr5234.

27. H.-S. Lai, Y.-C. Zhou, Z.-Q. Sun, C. He, and Y.-F. Chen, "Photonic Axion Insulator With Non-Coplanar Chiral Hinge Transport," *Nature Communications* 16, no. 1 (2025): 3826, https://doi.org/10.1038/s41467-025-59214-2.

28. M. Wang, R.-Y. Zhang, L. Zhang, et al., "Topological One-Way Large-Area Waveguide States in Magnetic Photonic Crystals," *Physical Review Letters* 126, no. 6 (2021): 067401, https://doi.org/10.1103/PhysRevLett.126.067401.

29. Z. Li, S. Ma, S. Li, et al., "Observation of Copropagating Chiral Zero Modes in Magnetic Photonic Crystals," *Physical Review Letters* 134, no. 3 (2025): 033802, https://doi.org/10.1103/PhysRevLett.134.033802.

30. Q. Zhang, X. Xing, D. Zou, et al., "Investigation of Unidirectional Coupling of Dipole Emitters in Valley Photonic Heterostructure Waveguides," *Optics Express* 32, no. 1 (2023): 415–424, https://doi.org/10.1364/OE.510304.

31. P. Zhou, G.-G. Liu, Y. Yang, et al., "Observation of Photonic Antichiral Edge States," *Physical Review Letters* 125, no. 26 (2020): 263603, https://doi.org/10.1103/PhysRevLett.125.263603.

32. Z. Ji, J. Chen, and Z.-Y. Li, "Perspective: Antichiral Magnetic Topological Photonics," *Journal of Applied Physics* 133, no. 14 (2023): 140901, https://doi.org/10.1063/5.0144864.

33. E. Colomés and M. Franz, "Antichiral Edge States in a Modified Haldane Nanoribbon," *Physical Review Letters* 120, no. 8 (2018): 086603.

34. J. Chen and Z.-Y. Li, "Prediction and Observation of Robust One-Way Bulk States in a Gyromagnetic Photonic Crystal," *Physical Review Letters* 128, no. 25 (2022): 257401, https://doi.org/10.1103/PhysRevLett.128.257401.

35. Y. Zheng, J. Chen, Z. Ji, and Z.-Y. Li, "Continuously Tunable Topological Negative Refraction via a Tailorable Bloch Wavevector in Momentum Space," *Photonics Research* 13, no. 8 (2025): 2159–2171, https://doi.org/10.1364/PRJ.560388.

36. H. Wang, B. Xie, and W. Ren, “Coexistence of Chiral and Antichiral Edge States in Photonic Crystals,” *Laser & Photonics Reviews* 18, no. 1 (2024): 2300764, https://doi.org/10.1002/lpor.202300764.

37. S. Liu, Y. Yang, L. Shi, E. Wang, and Z. H. Hang, “Chiral and Antichiral Edge States in Gyromagnetic Photonic Crystals Under Magnetic and Pseudomagnetic Fields,” *Photonics Research* 13, no. 9 (2025): 2688–2696, https://doi.org/10.1364/PRJ.568411.

38. Y.-C. Zhou, Z.-Q. Sun, H.-S. Lai, X.-C. Sun, C. He, and Y.-F. Chen, “Observation of Photonic Chern Metal With Bi-Chiral Edge Propagation,” *Laser & Photonics Reviews* 18, no. 12 (2024): 2400826, https://doi.org/10.1002/lpor.202400826.

39. X. Ni, D. Purtseladze, D. A. Smirnova, A. Slobozhanyuk, A. Alù, and A. B. Khanikaev, “Spin-and Valley-Polarized One-Way Klein Tunneling in Photonic Topological Insulators,” *Science advances* 4, no. 5 (2018): aap8802, https://doi.org/10.1126/sciadv.aap8802.

40. X. Cui, R.-Y. Zhang, Z.-Q. Zhang, and C. T. Chan, “Photonic Z_2 Topological Anderson Insulators,” *Physical Review Letters* 129, no. 4 (2022): 043902, https://doi.org/10.1103/PhysRevLett.129.043902.

41. J.-W. Liu, F.-L. Shi, K. Shen, et al., “Antichiral Surface States in Time-Reversal-Invariant Photonic Semimetals,” *Nature Communications* 14, no. 1 (2023): 2027, https://doi.org/10.1038/s41467-023-37670-y.

42. G. Yu, J. Xia, L. Lai, et al., “Klein-Tunneling Increases the Signal Modulation Rate of Elastic Wave Systems,” *International Journal of Mechanical Sciences* 253 (2023): 108412, https://doi.org/10.1016/j.ijmecsci.2023.108412.

43. M. Wang, R.-Y. Zhang, C. Zhang, et al., “Three-Dimensional Nonreciprocal Transport in Photonic Topological Heterostructure of Arbitrary Shape,” *Science Advances* 11, no. 2 (2025): adq9285, https://doi.org/10.1126/sciadv.adq9285.

Supporting Information

Additional supporting information can be found online in the Supporting Information section.

Supporting File: lpor71603-sup-0001-SuppMat.pdf.